



Methanation of CO₂ on iron based catalysts



Johann Kirchner, Jasmin Katharina Anolleck, Henry Lösch, Sven Kureti*

Technical University of Freiberg, Institute of Energy Process Engineering and Chemical Engineering, Chair of Reaction Engineering, Fuchsmuehlenweg 9, D-09599 Freiberg, Germany

ARTICLE INFO

Article history:

Received 28 November 2016
Received in revised form 30 May 2017
Accepted 8 June 2017
Available online 9 June 2017

Keywords:

Catalytic methanation
Catalytic CO₂ hydrogenation
Iron oxide
Iron carbide
Carbon deposit

ABSTRACT

In this paper, several bare iron oxide samples were investigated for catalytic hydrogenation of CO₂ to CH₄ and H₂O under atmospheric pressure. The fresh samples were thoroughly characterised by N₂ physisorption, X-ray diffraction (XRD) and Moessbauer spectroscopy. Hydrogenation studies were performed with a CO₂ fraction of 1000 ppm and a molar H₂/CO₂ ratio of 200 to accurately monitor gas phase species providing reliable mass balance of carbon. The obtained results evidenced reduction of the iron oxides followed by significant accumulation of carbon. In situ XRD and temperature-programmed hydrogenation (TPH) demonstrated formation of iron carbide (θ-Fe₃C) as well as carbonaceous deposits implying surface and bulk carbon entities. The quantity of each carbon species depended on the physical-chemical properties of the catalysts with fast carburisation of relatively large iron crystallites originated from iron oxide reduction.

The best methanation activity was found for nano-sized γ-Fe₂O₃ indicating maximum CH₄ yield of ca. 60% at 400 °C. TPH analyses suggested that the hydrogenation efficiency of this catalyst was mainly associated with reactive surface carbon species.

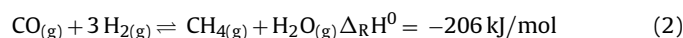
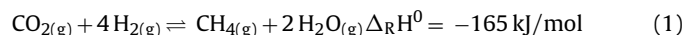
Furthermore, for more practical assessment of γ-Fe₂O₃, CO₂ hydrogenation was conducted with a CO₂ proportion of 10 vol.% and stoichiometric H₂/CO₂ ratio leading to decreased yield of CH₄ and predominate formation of CO. Based on XRD, TPH and Moessbauer spectroscopic analyses the catalytic activity under these conditions was ascribed to θ-Fe₃C and χ-Fe₅C₂ entities with some contribution of carbon species deposited on the catalyst.

© 2017 Elsevier B.V. All rights reserved.

1. Introduction

Technological progress as well as worldwide industrialisation led to rapid growth of global energy consumption, which nearly doubled during the past 20 years [1]. The energy utilisation is mainly based on fossil fuels predominantly including coal, petroleum and natural gas [2]. As a consequence, CO₂ is produced causing global warming [3]. Atmospheric CO₂ content continuously increased from 316 ppm in 1959–400 ppm in 2015 [4]. Thus, the reduction of the anthropogenic CO₂ output becomes a global issue. In this context, Carbon Capture and Storage (CCS) is widely discussed implying separation of CO₂ from flue gases and subsequent underground storage [5]. Additionally, many efforts were made for Carbon Capture and Utilisation (CCU) taking CO₂ as a carbon source in the synthesis of chemicals and fuels [2,6–8]. A possible route is the catalytic hydrogenation of carbon dioxide to methane and water as explored by Sabatier and Senderens at first (Eq. (1)) [9].

This process includes the production of synthetic natural gas (SNG) as well as chemical storage of hydrogen. Several methanation pilot plants are already operating in practice such as Audi's power-to-gas facility in Germany yielding SNG from renewable hydrogen and biogenic CO₂ [10] or the KIC project "DemoSNG" combining the power-to-gas process with biomass gasification [11]. Moreover, SNG can be obtained from the methanation of carbon monoxide as well (Eq. (2)). Beside the production of SNG, methanation is already a state-of-the-art technology for the elimination of carbon oxides in hydrogen production, e.g. in the purification of ammonia synthesis gas [12].



Eqs. (1) and (2) indicate that the CO_x methanation is a reversible and strongly exothermic reaction, which reduces the number of molecules involved. Therefore, high thermodynamic yields appear with decreasing temperature and increasing pressure. Consequently, mainly multi-stage reactor systems were developed operating at temperatures below 500 °C and pressures up to 20 bar

* Corresponding author.

E-mail address: kureti@iec.tu-freiberg.de (S. Kureti).

[12]. Furthermore, as a side reaction of methanation the water gas shift (WGS) reaction occurs (Eq. (3)) affecting the CO/CO₂ ratio upon hydrogenation.



For the methanation of CO₂ and CO, Ni based catalysts are widely considered due to their high activity as well as selectivity towards CH₄. These catalysts are primarily supported by high surface area carriers such as Al₂O₃, SiO₂, CeO₂ and TiO₂ [13–15]. For instance, Mutz et al. [16] reported on a Ni/CaO–Al₂O₃ catalyst with a Ni content of 23 wt.%. When using a stoichiometric H₂/CO₂ ratio, high CO₂ conversion (81%) and CH₄ selectivity (99%) was achieved at 400 °C under atmospheric pressure. Similar results were shown by Rahmani et al. [17] investigating a Ni/γ-Al₂O₃ catalyst loaded with 20 wt.% Ni. At 350 °C and atmospheric pressure a CO₂ conversion of 82% with selective formation of CH₄ was obtained. Furthermore, other group VIII metals were studied for carbon oxide methanation as well, particularly Ru [18–20], Rh [21–23], Co [24,25] and Fe [26–29]. Ru based catalysts are known to be more active than Ni, but are significantly more expensive [30].

Mechanistic examinations indicate that CO is an important intermediate in the formation of CH₄ from CO₂ and H₂ [13,31]. This implies direct dissociation of CO₂ into O and CO on the catalysts followed by stepwise hydrogenation to CH₄. This type of mechanism is suggested for Rh/γ-Al₂O₃ [32] and Ni(100) catalysts [33]. Additionally, an alternative route discussed includes the adsorption of CO₂ and subsequent reaction with chemisorbed H leading to formate species (COOH). This pathway is proposed for Ru/TiO₂ [34] and Ni/ZrO₂ catalysts [35].

Despite their efficiency, traditional Ni based catalysts suffer from several disadvantages like deactivation due to sintering of Ni particles associated with the heat evolution upon methanation [36], deposition of coke and leaching of toxic nickel carbonyls as well as the toxicological concern of Ni itself [13,37]. In contrast to nickel, iron based catalysts benefit from a relatively low price and toxicological harmlessness. Lee et al. [26] investigated iron catalysts for the hydrogenation of CO₂ evidencing a CH₄ yield up to 17% referring to 320 °C, 1 bar and a molar H₂/CO₂ ratio of 8. Also, increase in temperature and molar H₂/CO₂ ratio as well as decrease in space velocity enhance the CH₄ yield. Fournier et al. [29] reported a CH₄ yield of ca. 23% when using a Fe₂O₃ precursor for CO methanation at 290 °C and 1 bar. Recently, Hwang et al. [38] showed that the addition of Fe to Ni enhances stability and performance of the catalysts as compared to bare Ni. A CH₄ yield of about 63% was achieved at 220 °C and 10 bar on mesoporous alumina xerogel loaded with 35 wt.% Ni and 5 wt.% Fe.

Furthermore, iron catalysts are known to be active in the hydrogenation of carbon oxides to produce hydrocarbons according to the Fischer-Tropsch synthesis (FTS) [39]. FTS catalyst precursors mainly comprise nano-scaled Fe₂O₃ crystallites and promotor components, particularly copper for catalyst reducibility, K₂O for CO dissociation and silica or zinc oxide for iron dispersion [40]. Moreover, iron oxides are also known to be active in the high temperature water-gas shift reaction (Eq. (3)). These catalysts mainly consist of Fe₃O₄ and Cr₂O₃ and operate in a temperature range from 310 °C to 450 °C [41]. Besides, Fe₃O₄ is used as catalyst precursor for the ammonia synthesis promoted by K₂O, CaO, Al₂O₃ and SiO₂ [42].

It is well known that iron based catalysts undergo complex phase changes during CO_x hydrogenation [43,44]. Iron oxides (Fe₂O₃, Fe₃O₄ or FeO), metallic iron and iron carbides (ε-Fe₂C, ε'-Fe₂C₂, χ-Fe₅C₂, θ-Fe₃C) were found to coexist. Due to the complex iron-carbon-oxygen system and its dynamic behaviour under syngas conditions the exact structure of the active sites in Fischer-Tropsch synthesis or CO_x methanation is not yet unambiguously identified and is controversially discussed [40]. In addition to iron,

carbonaceous species formed on the catalyst are also of relevance. Bartholomew [45] differentiated adsorbed atomic carbon (C_α), polymeric surface carbon (C_β), iron carbides (C_γ) and graphitic carbon (C_δ) each showing specific activity in CO_x hydrogenation. Xu et al. [46] and Herranz et al. [47] supported the importance of C_α and C_β upon methanation, but also supposed both species to form carbides. Additionally, the conversion of surface carbon to less reactive graphitic carbon was discussed to occur at high temperatures and long time on stream (TOS) [45].

Moreover, high catalytic activity of iron based catalysts was also reported for O₂ rich operation conditions, particularly in the aftertreatment of diesel exhaust. For instance, Fe/BEA zeolites are efficient in the selective catalytic reduction of NO_x by NH₃ [48], while Fe₂O₃ and Fe₃O₄ catalysts were evaluated for CO and soot oxidation, respectively [49].

The present paper deals with the CO₂ methanation using different iron oxides as catalyst precursors in order to investigate the effect of iron phase and potentially formed carbonaceous species on the performance. The iron oxide samples were physical-chemically characterised by N₂ physisorption, X-ray diffraction (XRD) and Moessbauer spectroscopy, whereas their activity was tested at atmospheric pressure between 250 °C and 450 °C. In the catalytic tests, a molar H₂/CO₂ feed ratio of 200 with a CO₂ fraction of 1000 ppm was taken to quantify carbon deposits by balancing the mass of gaseous compounds. Furthermore, phase transformations upon methanation were examined by in situ XRD, while for more detailed investigation of carbonaceous species temperature-programmed hydrogenation (TPH) was made after methanation. Finally, methanation tests with higher CO₂ amount as well as stoichiometric H₂/CO₂ ratio were performed to check technical relevance.

2. Experimental

2.1. Preparation and characterisation of catalysts

Six different iron oxide powder catalysts were investigated, whereas five samples were commercially available and one was home-made. The catalysts implied nano-sized γ-Fe₂O₃ (Sigma-Aldrich, 98%, particle size <50 nm), γ-Fe₂O₃ (Lanxess, 99.5%), Fe₃O₄ (Lanxess, 98%), FeO (Chempur, 99.5%), nano-sized α-Fe₂O₃ (Chempur, 99%, particle size <40 nm) and α-Fe₂O₃ (self-prepared). For differentiation of both γ-Fe₂O₃ powders, the sample from Sigma-Aldrich is denoted as γ-Fe₂O₃(n) due to its nano-ranged particle size. The home-made α-Fe₂O₃ sample referred as α-Fe₂O₃(PVA) was prepared by polyvinyl alcohol (PVA) route as recently demonstrated in detail [50]. Briefly, an aqueous PVA solution (Merck, 98%, molecular weight: ca. 145'000 g/mol) with 9 wt.% PVA and an iron nitrate solution were mixed, whereas the molar ratio of Fe³⁺ cations to VA monomer units was 2.5. The solution was slowly heated and evaporated under continuous stirring. After this, the remaining residual was dried at 250 °C and was finally calcined in flowing air at 600 °C for 5 h [51].

The crystalline structure of the samples was analysed by powder X-ray diffraction on a D8 Discover (Bruker-AXS) with Co-Kα radiation. The diffractogram was recorded from 15° to 90° in 2θ mode with a step width of 0.051° using a VANTEC-1 detector. The crystallite size (d) was estimated by taking the Scherrer equation $d = \frac{K\lambda}{B \cos \theta}$, where K is a dimensionless shape factor (taken as 0.92), λ is the wavelength of X-ray, B refers to the full width at half maximum (FWHM) in radians and θ is the Bragg angle [52]. For in situ XRD studies, a high temperature cell (TC-radiation, Bruker-AXS) with polyimide windows (Kapton) was used allowing the supply of gases. Furthermore, a 2-D detector (VANTEC-2000) was taken simultaneously recording an angular range of 30°. In the in situ XRD measurements, a total gas flow of 200 ml min⁻¹ was established. A

catalyst mass of ca. 50 mg was placed on the corundum sample holder and was heated to 400 °C in flowing N₂ by the radiant Pt-Rh heater. The temperature was controlled by S-type thermocouple located ca. 1 mm above the crucible. Subsequently, a H₂/N₂ mixture (10 vol.% H₂, 90 vol.% N₂) was adjusted until complete reduction to metallic iron was observed. After this, the reaction mixture consisting of 1000 vppm CO₂, 20 vol.% H₂ and N₂ balance was fed to the chamber heated to 400 °C and then diffractograms were recorded. The total acquisition time of one diffraction pattern was 6 min resulting from the three sub-ranges consecutively scanned, i.e. 10–40°, 35–65° and 60–90°. Quantitative phase composition was evaluated by TOPAS software (Bruker-AXS) employing standard fitting procedure according to the Rietveld refinement [53]. The respective R_{wp} factors, which characterise the fitting results, were below 5.0 for each fit [54].

The specific surface area (BET) and pore size distribution of the catalysts was deduced from the N₂ adsorption/desorption isotherms taken at –196 °C on a TriStar II (Micromeritics). Prior to N₂ exposure, respective sample was outgassed in vacuum (10^{–1} mbar) at 350 °C for 16 h to remove adsorbed components, particularly H₂O. The BET surface area was derived from the adsorption data recorded at p/p₀ ratios ranging from 0.05 to 0.2. The pore size distribution was calculated from the desorption data using the Barrett Joyner Halenda (BJH) approach [55].

⁵⁷Fe Moessbauer spectroscopy was conducted by using a 100 mCi ⁵⁷Co source in a Rh matrix. The spectrometer (WissEl) was operated in constant acceleration mode. The spectra were taken at ambient conditions with a moving source and a fixed sample using a proportional counter. The experimental Moessbauer spectra were deconvoluted by least-square fitting procedure taking Lorentzian peak shapes. The obtained correlation coefficients were always above 0.95 indicating appropriate validity of deconvolution. Isomer shift, quadrupole splitting and hyperfine field are reported relative to α-Fe.

2.2. Catalytic studies and temperature-programmed hydrogenation

The catalytic methanation studies were conducted on a laboratory test bench equipped with a fixed-bed quartz tube reactor (i.d. 8 mm). The measurements were made at atmospheric pressure in the temperature regime from 250 to 450 °C. Before the tests, respective sample was pressed to pellet, granulated and sieved to a size of 125–250 μm to avoid discharge in the catalytic tests. Then, a catalyst mass of 200 mg was fixed in the reactor by quartz wool and pretreated in flowing nitrogen at 450 °C for 1 h to eliminate possible impurities, e.g. adsorbed H₂O and CO₂. The temperature was monitored by two K-type thermocouples directly placed in front of and behind the fixed-bed. In some runs, respective catalyst was subsequently activated at 450 °C for 2 h by adding a blend of 20 vol.% H₂ and 80 vol.% N₂ at a total flow of 500 ml min^{–1}. Finally, the methanation mixture was adjusted comprising 1000 vppm CO₂ and 20 vol.% H₂ (N₂ balance) corresponding to a molar H₂/CO₂ ratio of 200. Additional studies were performed with a stoichiometric H₂/CO₂ ratio of 4 and a CO₂ proportion of 10 vol.%. The total gas flow was kept at 500 ml min^{–1} resulting in a space velocity of 120,000 h^{–1}. All the gases (Air Liquide) were fed from independent mass flow controllers (Bronkhorst). The reactor effluents (CO₂, CO, CH₄, C₂H₆, C₂H₄, C₃H₈, C₃H₆ and H₂O) were continuously monitored by a hot measuring MultiGas 2030 FTIR spectrometer (MKS Instruments). The stainless steel pipes of the bench were held at 120 °C to avoid condensation of H₂O.

The performance of the catalysts is expressed in terms of conversion of CO₂ ($X_{\text{CO}_2} = (Y_{\text{CO}_2,\text{in}} - Y_{\text{CO}_2,\text{out}}) / Y_{\text{CO}_2,\text{in}}$) as well as selectivity of CH₄ (S_{CH_4}) and CO (S_{CO}): $S_i = Y_{i,\text{out}} / (Y_{\text{CO}_2,\text{in}} - Y_{\text{CO}_2,\text{out}})$,

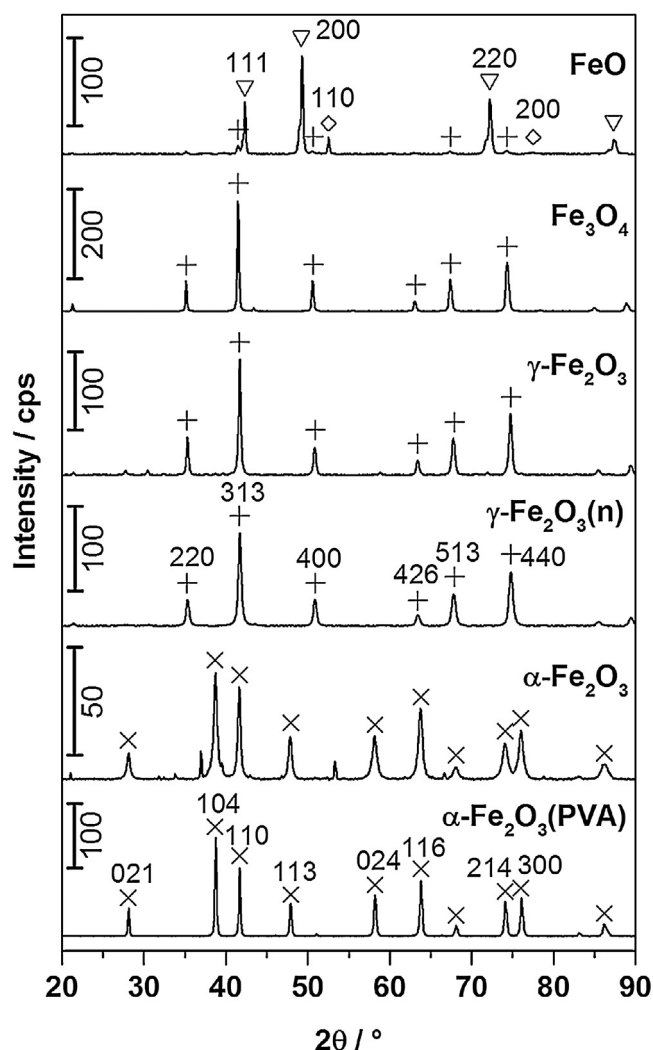


Fig. 1. XRD patterns of the iron oxide samples; the reflexes are assigned to crystalline phases of α-Fe₂O₃ (×), γ-Fe₂O₃/Fe₃O₄ (+), Fe⁰ (◇) and FeO (∇).

where i is CH₄ and CO, respectively. Also, the yield of CH₄ ($Y(\text{CH}_4) = Y_{\text{CH}_4,\text{out}} / Y_{\text{CO}_2,\text{in}}$) is used. Due to the relatively small fraction of CH₄ formed the overall flow rate is not significantly influenced in the catalytic experiments.

Temperature-programmed hydrogenation (TPH) was performed for the characterisation of carbonaceous species potentially formed upon CO₂ hydrogenation. For this purpose, respective catalyst was flushed with N₂ directly after methanation study and was cooled rapidly to room temperature. After this, pure H₂ was dosed at a flow rate of 200 ml min^{–1}, while TPH was started by linearly increasing the temperature to 800 °C with a ramp of 5 K min^{–1}. As for CO₂ methanation, reactor effluents were analysed by FTIR.

3. Results and discussion

3.1. Characterisation of the catalysts

The XRD patterns of the as-prepared catalysts (Fig. 1) indicate high purity of the existing iron oxide phases without any presence of amorphous domains as evidenced by Rietveld refinement. But, it has to be stated that the differentiation of γ-Fe₂O₃ and Fe₃O₄ by XRD is difficult, since lattice parameters and crystalline structures closely resemble resulting in very similar diffractograms. For the α-Fe₂O₃ sample, hematite-type structure is confirmed as major

Table 1

Crystallite size (d), BET surface area (S_{BET}), total pore volume (V_{pore}) and average pore size (d_{pore}) of the iron oxide samples.

Sample	d/nm ^a	$S_{\text{BET}}/\text{m}^2 \text{g}^{-1}$ ^b	$V_{\text{pore}}/\text{cm}^3 \text{g}^{-1}$ ^b	$d_{\text{pore}}/\text{nm}$ ^b
$\alpha\text{-Fe}_2\text{O}_3(\text{PVA})$	68	9	0.063	46
$\alpha\text{-Fe}_2\text{O}_3$	17	19	0.057	29
$\gamma\text{-Fe}_2\text{O}_3(\text{n})$	21	42	0.204	33
$\gamma\text{-Fe}_2\text{O}_3$	34	28	0.064	34
Fe_3O_4	65	5	0.008	38
FeO	61	<1		

^a Estimated from XRD according to Scherrer equation.

^b Derived from N_2 physisorption.

phase, whereas weak reflexes at 37.1° , 53.4° and 66.8° related to halite-type phase (NaCl) are also observed. The minor presence of sodium is corroborated by X-ray fluorescence and is likely associated with the special synthesis route [56,57]. Additionally, the XRD pattern of the FeO sample substantiates predominate existence of FeO with some contribution of Fe_3O_4 and elemental Fe. The later components are ascribable to the thermodynamic decomposition of FeO below 570°C ($\text{FeO} \rightarrow \text{Fe}_3\text{O}_4 + \text{Fe}$) [58]. From the Rietveld refinement a proportion of 84 wt.% FeO, 10 wt.% Fe_3O_4 and 6 wt.% Fe is deduced. Furthermore, the FeO reflexes all reveal a shoulder on the low 2θ side attributed to wuestite-type phases with different stoichiometry. It is well known that due to cation vacancies and structural defects wuestite-type phase generally implies a wide range of non-stoichiometric compositions according to the formula Fe_{1-x}O , where x ranges from 0.05 to 0.15 [59–61].

Moreover, the crystallite sizes of the prevalent phases estimated from the diffractograms by Scherrer equation are demonstrated in Table 1. The $\alpha\text{-Fe}_2\text{O}_3$ and $\gamma\text{-Fe}_2\text{O}_3(\text{n})$ samples show relatively small crystallites (17 nm and 21 nm, respectively) in agreement with the manufacturers' data. Contrary, the largest crystallite size is found for $\alpha\text{-Fe}_2\text{O}_3(\text{PVA})$ (68 nm).

The Moessbauer spectra of the fresh iron oxide samples are demonstrated in Fig. 2. The isomer shift, quadrupole splitting and magnetic hyperfine field (Table 2) derived from spectral deconvolution are in good accordance with characteristics reported in literature [62]. The Moessbauer features of $\alpha\text{-Fe}_2\text{O}_3(\text{PVA})$, $\gamma\text{-Fe}_2\text{O}_3$ and $\gamma\text{-Fe}_2\text{O}_3(\text{n})$ are each described by one typical sextet substantiating the exclusive presence of $\alpha\text{-Fe}_2\text{O}_3$ and $\gamma\text{-Fe}_2\text{O}_3$, respectively, in line with XRD. Also, the spectrum of Fe_3O_4 sample corresponds to that expected for inverse spinel-type Fe_3O_4 implying two sextets due to tetrahedral and octahedral lattice sites. The FeO sample reveals two duplets related to wuestite-type structures with slightly different coordination of the Fe^{2+} sites [63]. The duplex with high isomer shift (1.00 mm s^{-1}) and smaller quadrupole splitting (0.29 mm s^{-1}) indicates higher symmetry of the octahedrally coordinated Fe^{2+} sites rather attributed to stoichiometric FeO. Contrary, the high quadrupole splitting of the other duplex (0.76 mm s^{-1}) suggests a less ordered structure thus referring to non-stoichiometric Fe_{1-x}O [60,64]. Additionally, two sextets typical for Fe_3O_4 also

appear in the FeO sample corresponding to a fraction of ca. 13 wt.%. This result agrees well with the quantitative XRD analysis showing a Fe_3O_4 proportion of about 10 wt.%. However, in contrast to XRD, elemental iron is not proven by Moessbauer spectroscopy, which might be associated with its minor abundance. For the $\alpha\text{-Fe}_2\text{O}_3$ sample, an additional duplex is found beside the expected sextet of $\alpha\text{-Fe}_2\text{O}_3$. Based on the isomer shift (0.29 mm s^{-1}) and quadrupole splitting (0.67 mm s^{-1}) this feature may be attributed to superparamagnetic (spm) ferric oxide species smaller than ca. 20 nm [62,65]. This interpretation is additionally supported by the crystallite size estimated from XRD (17 nm).

The results from N_2 physisorption are presented in Table 1. For FeO total pore volume and average pore size is not available due to its little N_2 uptake associated with very low BET surface area ($<1 \text{ m}^2 \text{g}^{-1}$). Contrary, the $\gamma\text{-Fe}_2\text{O}_3(\text{n})$ sample reveals the highest BET surface area ($42 \text{ m}^2/\text{g}$) as well as largest total pore volume ($0.204 \text{ cm}^3/\text{g}$). Basically, the iron oxide catalysts reasonably show decreasing total pore volume and increasing average pore size with inclining BET surface area. The pore size distributions according to BJH show pores within a relative broad regime between 5 and 100 nm, whereas the average pore diameters lie in the mesoporous range (Table 1). The N_2 adsorption/desorption isotherms (Fig. 3) are referred to type IV as classified by Brunauer et al. [66] thus confirming mesoporosity of the samples [67]. Besides, $\alpha\text{-Fe}_2\text{O}_3$ is characterised by a bimodal mesoporous structure with pore sizes from 3 to 4 nm and from 15 to 70 nm. This pore size distribution is also in line with the measured shape of N_2 isotherm, which is typical for H3-type hysteresis assignable to mesopores surrounded by a matrix of much smaller pores [68]. Furthermore, $\gamma\text{-Fe}_2\text{O}_3(\text{n})$, $\alpha\text{-Fe}_2\text{O}_3(\text{PVA})$ and $\gamma\text{-Fe}_2\text{O}_3$ exhibit H1-type hysteresis usually attributed to rather uniform cylindric pores [69,70].

3.2. Thermodynamics of the $\text{CO}_2\text{-H}_2$ reaction

The thermodynamics of the CO_2 methanation were calculated by CHEMCAD 7 (Chemstations) software using Gibbs free energy minimisation. The results are shown in Fig. 4 for the two relevant reaction mixtures implying CO_2/H_2 ratios of 0.1 vol.%/20 vol.% and 10 vol.%/40 vol.% at a total pressure of 1 bar. In the calculations, gaseous CO_2 , CO, CH_4 and H_2O as well as solid graphitic carbon were considered. The equilibrium composition of the reaction mixture with 0.1 vol.% and 20 vol.% shows complete conversion of CO_2 into CH_4 in the whole temperature range with temperature-independent fractions of the reactants referred to the very high excess of H_2 . On the contrary, for the stoichiometric CO_2/H_2 mixture the abundance of CH_4 decreases with increasing temperature. Moreover, the CO proportion increases with rising temperature. For both reaction mixtures, no formation of carbon appeared in the entire temperature range.

Table 2

Moessbauer parameters of the iron oxide samples including isomer shift (δ), quadrupole splitting (E_Q) and hyperfine field (H_{hf}).

Sample	$\delta/\text{mm s}^{-1}$	$E_Q/\text{mm s}^{-1}$	H_{hf}/kOe	Fraction/wt. %	Assignment
$\alpha\text{-Fe}_2\text{O}_3(\text{PVA})$	0.37	−0.21	516	100	$\alpha\text{-Fe}_2\text{O}_3$
$\alpha\text{-Fe}_2\text{O}_3$	0.37	−0.21	512	93	$\alpha\text{-Fe}_2\text{O}_3$
	0.29	0.67		7	spm Fe_2O_3
$\gamma\text{-Fe}_2\text{O}_3(\text{n})$	0.32	−0.01	493	100	$\gamma\text{-Fe}_2\text{O}_3$
$\gamma\text{-Fe}_2\text{O}_3$	0.32	0.01	498	100	$\gamma\text{-Fe}_2\text{O}_3$
Fe_3O_4	0.30	−0.03	491	47	A site of Fe_3O_4
	0.64	−0.02	457	53	B site of Fe_3O_4
FeO	1.00	0.29		39	stoichiometric FeO
	0.91	0.76		48	non-stoichiometric Fe_{1-x}O
	0.18	−0.01	488	6	A site of Fe_3O_4
	0.70	−0.04	462	7	B site of Fe_3O_4

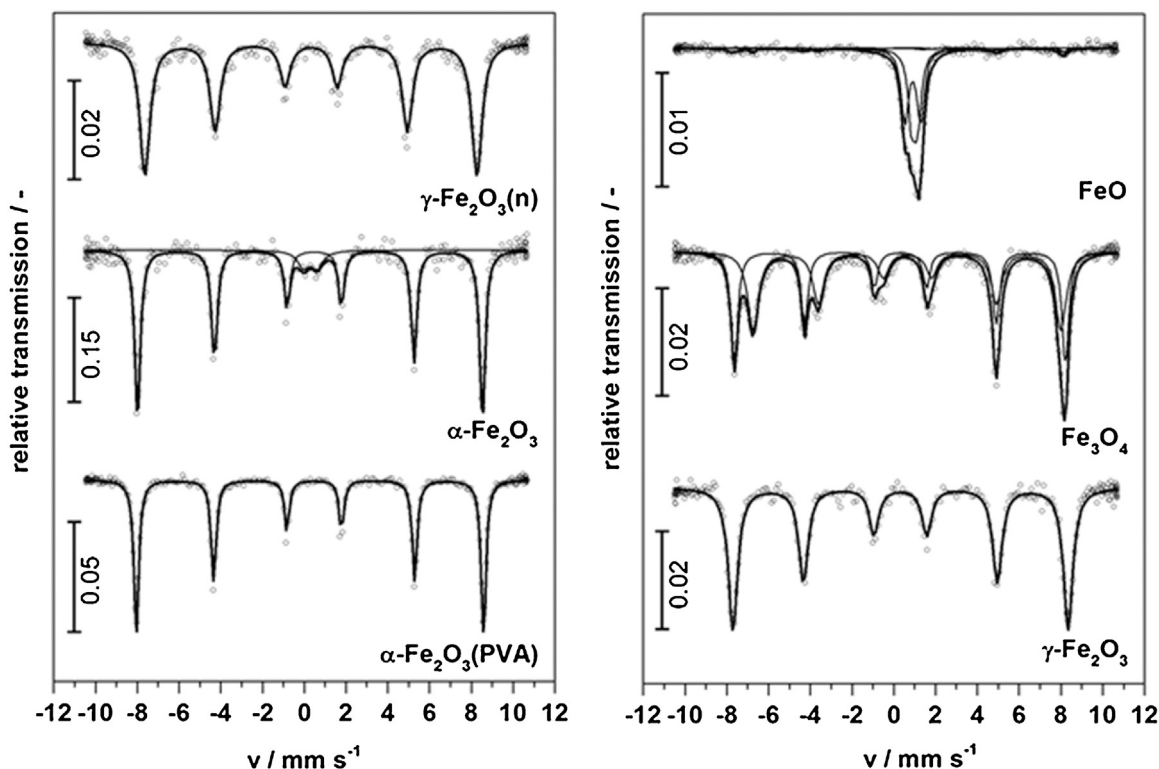


Fig. 2. Mössbauer spectra of the iron oxide samples at room temperature with deconvoluted sub-bands.

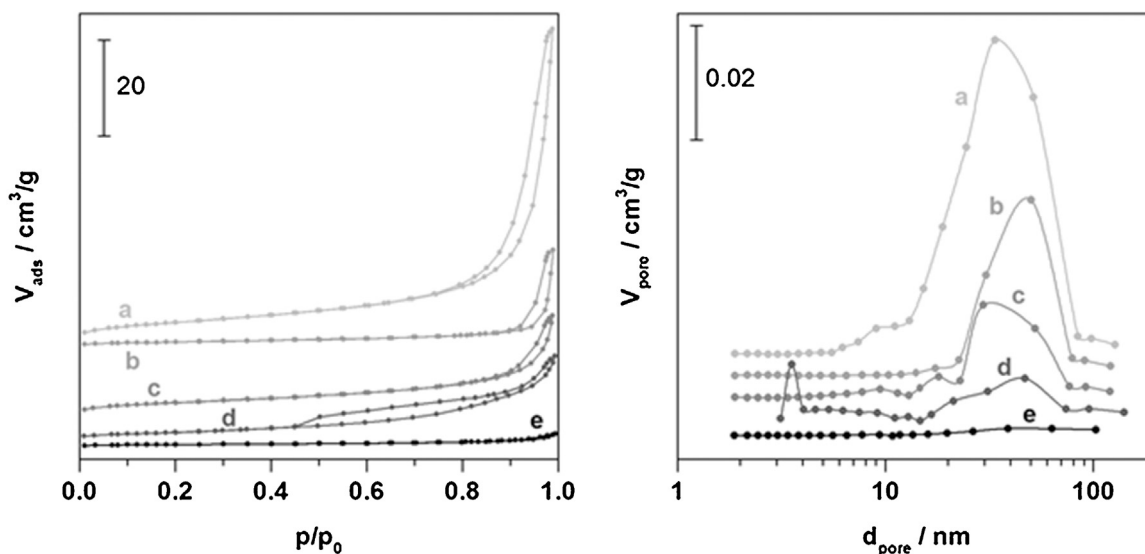


Fig. 3. N₂ adsorption-desorption isotherms (left) and BJH pore size distribution (right) of (a) γ -Fe₂O₃(n), (b) α -Fe₂O₃(PVA), (c) γ -Fe₂O₃, (d) α -Fe₂O₃ and (e) Fe₃O₄.

3.3. CO₂ methanation activity of the catalysts

For comparison purposes, the CO₂ hydrogenation activity of the iron oxide samples was evaluated at 350 °C by taking a molar CO₂/H₂ ratio of 200 and atmospheric pressure (Fig. 5). In these tests, the time on stream was kept at 120 min reaching or closely approaching steady state conditions. Also, the samples were not activated by a special pretreatment to investigate possible phase transformations and activity changes in methanation. Substantial CH₄ production was expected under the test conditions taken as derived from a related FTS study on Fe based catalysts [71]. Note that no CO₂ hydrogenation occurred in the absence of a catalyst.

In the catalytic methanation tests, CH₄ and CO are the only carbon containing products found in gas phase. Note that higher hydrocarbons such as ethane, ethene, propane and propene as well as methanol, which are basically detectable by the FTIR spectrometer in an unambiguous manner, are not observed. The difference of inlet and outlet temperature is always smaller than 10 K and no pressure drop occurs during time on stream. Furthermore, all the catalysts follow a similar trend characterised by little formation of CH₄ in the beginning combined with strong yield of CO (Fig. 5) according to RWGS (Eq. (3)). Subsequently, the production of CO decreases, while the conversion of CO₂ as well as selectivity of

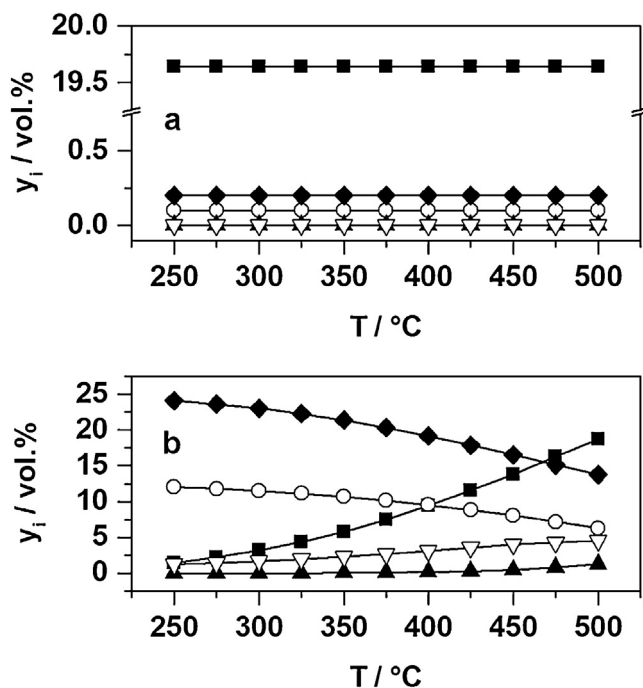


Fig. 4. Equilibrium composition of the CO_2 methanation reaction ($\text{H}_2(\text{g})$ (■), $\text{CH}_4(\text{g})$ (○), $\text{CO}(\text{g})$ (▲), $\text{CO}_2(\text{g})$ (▽), $\text{H}_2\text{O}(\text{g})$ (◆)). Reaction mixtures: (a) $y(\text{CO}_2) = 0.1 \text{ vol.}\%$, $y(\text{H}_2) = 20 \text{ vol.}\%$, (b) $y(\text{CO}_2) = 10 \text{ vol.}\%$, $y(\text{H}_2) = 40 \text{ vol.}\%$; N_2 balance; $p = 1 \text{ bar}$.

CH_4 increase. The highest CH_4 selectivity is obtained for $\gamma\text{-Fe}_2\text{O}_3(\text{n})$ amounting to 87% at a CO_2 conversion of ca. 67%.

For each sample, the mass balance of carbon was calculated by using the following equation: $\Delta n_{\text{C}} = \dot{V} V_{\text{m}}^{-1} \int_0^t (y(\text{CO}_2)_{\text{in}} - y(\text{CO}_2)_{\text{out}} - y(\text{CO})_{\text{out}} - y(\text{CH}_4)_{\text{out}}) dt$, t is the time on stream, \dot{V} the total gas flow and V_{m} the molar gas volume. Fig. 6 evidences significant disparity between the quantity of inflowing

and outflowing carbon suggesting continuous accumulation on all the catalysts. This effect is associated with formation of iron carbides and carbon deposits and is discussed in detail in Section 3.5. Additionally, the quantity of accumulated carbon strongly depends on the catalyst. The highest carbon deposition is observed for $\alpha\text{-Fe}_2\text{O}_3(\text{PVA})$ showing an abundance of ca. $625 \mu\text{mol}$ after a TOS of 120 min. Furthermore, from correlation of the mass of carbon deposited (Fig. 6) with the methanation data (Fig. 5) it is evident that the CO selectivity decreases when the carbon accumulation begins. The high CO formation at the beginning of CO_2 hydrogenation is attributed to RWGS (Eq. (3)) catalysed by iron oxide as reported in the literature [72]. With increasing TOS the catalyst is reduced due to the excess presence of hydrogen followed by carburisation. As a result, the CO selectivity progressively declines accompanied with growing production of CH_4 . Based on these features it is assumed that the reduced catalyst, particularly metallic iron, as well as iron carbides are clearly more active in CO_x methanation than the iron oxides Fe_2O_3 , Fe_3O_4 and FeO . Finally, no correlation between physical-chemical properties of the as-prepared iron oxide samples, i.e. crystalline structure, oxidation state, BET surface area and porosity (Section 3.1), and catalytic performance is found. This is associated with the strong structural changes occurring upon methanation as discussed below.

3.4. CO_2 methanation on prereduced $\gamma\text{-Fe}_2\text{O}_3(\text{n})$ and $\alpha\text{-Fe}_2\text{O}_3(\text{PVA})$ catalysts

Additional hydrogenation studies were made with $\gamma\text{-Fe}_2\text{O}_3(\text{n})$, which reveals the best methanation performance, as well as $\alpha\text{-Fe}_2\text{O}_3(\text{PVA})$ evidencing strongest carbon accumulation (Section 3.3). The tests were performed from 250 to 450°C while prolonging the TOS to approx. 18 h. Before CO_2 hydrogenation, the catalysts were activated for 2 h at 450°C in a flowing blend of 20 vol.% H_2 and 80 vol.% N_2 , since iron oxide was shown to be not active in CH_4 production (Fig. 5). The reduction of the catalysts was followed

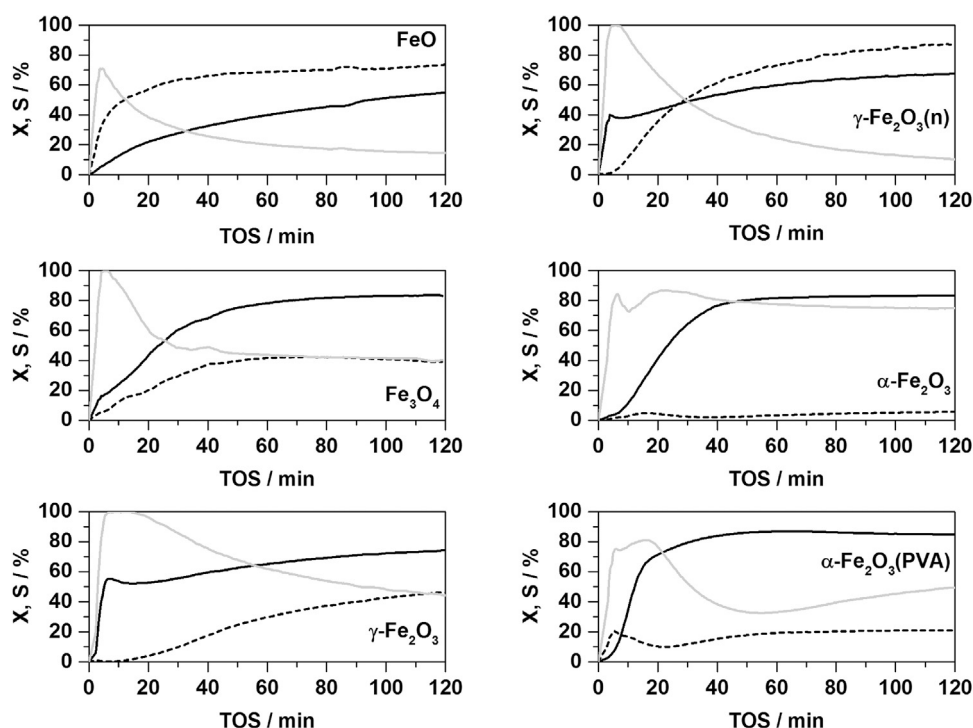


Fig. 5. CO_2 methanation activity of the iron oxide samples at 350°C without pretreatment ($X(\text{CO}_2)$ (—), $S(\text{CH}_4)$ (---), $S(\text{CO})$ (—)). Methanation conditions: $y(\text{CO}_2) = 1000 \text{ vppm}$, $y(\text{H}_2) = 20 \text{ vol.}\%$, N_2 balance, $\text{GHSV} = 120'000 \text{ h}^{-1}$, $p = 1 \text{ bar}$.

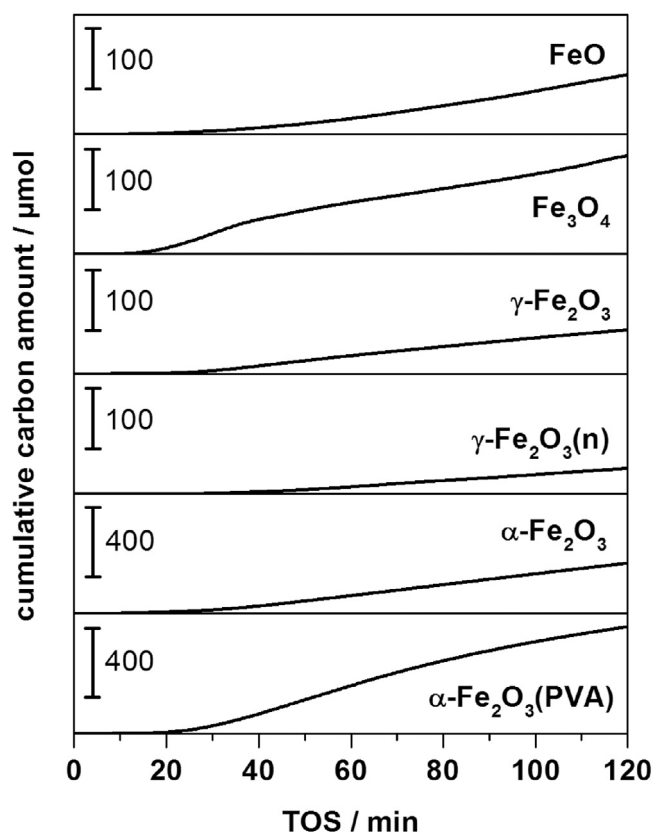


Fig. 6. Carbon accumulation on the iron oxide catalysts during CO_2 methanation at 350°C . Methanation conditions: $y(\text{CO}_2) = 1000$ vppm, $y(\text{H}_2) = 20$ vol.%, N_2 balance, GHSV = $120,000\text{ h}^{-1}$, $p = 1$ bar.

by monitoring H_2O confirming complete formation of elemental iron. As expected, after the H_2 pretreatment the starting CO formation (Fig. 7) is lower than that of the as-prepared catalysts (Fig. 5). However, for both samples, the yield of CH_4 obtained after 2 h is higher without initial exposure to H_2 (59% for $\gamma\text{-Fe}_2\text{O}_3(\text{n})$, 18% for $\alpha\text{-Fe}_2\text{O}_3(\text{PVA})$) as compared to that of the pretreated samples (28% and 6%). This indicates that the catalysts without preliminary H_2 exposure are increasingly activated during methanation in line with literature [73,74]. Particularly, Chun et al. reported on the activation of Fe/Cu/K/ SiO_2 based FTS catalysts by pretreatment with CO_2 containing feed leading to formation of reactive surface carbon and iron carbide species [75].

For the prereduced $\gamma\text{-Fe}_2\text{O}_3(\text{n})$ sample the initial CO_2 conversion increases with rising temperature achieving a maximum of ca. 65% at 450°C (Fig. 7, left). However, at this temperature CO_2 conversion goes down to about 28% with time on stream. Most prominent CO_2 conversion is observed at 400°C indicating only slight decrease; i.e. after 18 h the CO_2 conversion still equals to 45%, while the highest CH_4 yield is temporarily attained in the initial stage of methanation being 44%. The maximum CH_4 selectivity is obtained at 350°C (ca. 77%) accompanied with relatively low selectivity of CO (ca. 20%).

The $\alpha\text{-Fe}_2\text{O}_3(\text{PVA})$ sample shows a similar trend implying increase in CO_2 conversion with rising temperature (Fig. 7, right). The highest CO_2 conversion after 18 h (96%) is achieved at 450°C . But, at this temperature the initial CH_4 selectivity is relatively low with a maximum of only 4% after 3.5 h. Subsequently, the selectivity of CH_4 tentatively increases up to 7% after 18 h. Interestingly, conversion of CO_2 and selectivity of CH_4 slightly increase after ca. 8 h, which may be assigned to the formation of active carbonaceous species as discussed in Section 3.5. Highest CH_4 selectivity is found

at 400°C after 2.5 h (11%). As already stated, CO_2 is mainly converted into CO on the $\alpha\text{-Fe}_2\text{O}_3(\text{PVA})$ catalyst; between 250 and 450°C the CO selectivity is above 80%. The best yield of CH_4 is obtained at 400°C amounting to 9% only (after 2.5 h).

Note that in the performed hydrogenation tests the thermodynamic equilibrium (Fig. 4) is not reached associated with the high GHSV of $120,000\text{ h}^{-1}$ established in the fundamental studies.

3.5. Carbon accumulation on prereduced $\gamma\text{-Fe}_2\text{O}_3(\text{n})$ and $\alpha\text{-Fe}_2\text{O}_3(\text{PVA})$ catalysts

As done for the as-prepared catalysts, the carbon balance is analysed for the methanation studies (Fig. 7) performed with prereduced $\gamma\text{-Fe}_2\text{O}_3(\text{n})$ and $\alpha\text{-Fe}_2\text{O}_3(\text{PVA})$. The resulting data demonstrated in Fig. 8 indicate that carbon is accumulated immediately after dosing the feed in contrast to the as-prepared samples (Fig. 6). Moreover, $\alpha\text{-Fe}_2\text{O}_3(\text{PVA})$ shows stronger carbon accumulation between 250 and 450°C as compared to $\gamma\text{-Fe}_2\text{O}_3(\text{n})$ in line with the unreduced catalysts (Fig. 6). More specifically, the most prominent carbon deposition is observed for $\alpha\text{-Fe}_2\text{O}_3(\text{PVA})$ at 450°C amounting to ca. $3060\text{ }\mu\text{mol}$ after methanation, whereas $\gamma\text{-Fe}_2\text{O}_3(\text{n})$ reveals a proportion of about $645\text{ }\mu\text{mol}$ only. Basically, for both samples the total carbon accumulation increases with temperature.

For deeper insights into the carbon accumulation, in situ XRD measurements were conducted for $\gamma\text{-Fe}_2\text{O}_3(\text{n})$ and $\alpha\text{-Fe}_2\text{O}_3(\text{PVA})$, whereas quantitative phase analysis was made by Rietveld refinement. The investigations were performed at 400°C yielding highest methanation activity. Again, the samples were pretreated in a flow of 20 vol.% H_2 and 80 vol.% N_2 leading to complete reduction to $\alpha\text{-Fe}$ (Fig. 9), and then the feed was supplied. The diffractograms show that the Fe phase obtained from $\alpha\text{-Fe}_2\text{O}_3(\text{PVA})$ is continuously converted into iron carbide ($\theta\text{-Fe}_3\text{C}$) resulting in a fraction of 57% after 270 min (Fig. 10). From these results it is inferred that the carbon accumulation in the beginning of hydrogenation is mainly attributed to the formation of $\theta\text{-Fe}_3\text{C}$. Contrary, no changes in the reflexes of $\alpha\text{-Fe}$ originated from $\gamma\text{-Fe}_2\text{O}_3(\text{n})$ are detected thus excluding significant carburisation. These findings are consistent with the mass balance of carbon indicating strong carbon incorporation for $\alpha\text{-Fe}_2\text{O}_3(\text{PVA})$, whereas for $\gamma\text{-Fe}_2\text{O}_3(\text{n})$ it is rather weak. Quantification of the carbon accumulation of $\alpha\text{-Fe}_2\text{O}_3(\text{PVA})$ provides a quantity of $1015\text{ }\mu\text{mol}$ with relatively sharp increase between 0 and 3 h (Fig. 8). For complete production of Fe_3C proven by in situ XRD a quantity of ca. $830\text{ }\mu\text{mol}$ C is needed. Therefore, it is likely that entire transformation into $\theta\text{-Fe}_3\text{C}$ occurs within the first 3 h of methanation. Additional carbon accumulation is ascribed to the formation of surface as well as bulk carbon as discussed below. The crystallite size of metallic iron obtained from reduction of $\gamma\text{-Fe}_2\text{O}_3(\text{n})$ and $\alpha\text{-Fe}_2\text{O}_3(\text{PVA})$ is estimated by the Scherrer equation showing 23 nm and 41 nm, respectively. In CO_2 methanation, the crystallite size of metallic iron remains almost constant in both samples. According to Chernavskii et al. the rate of carburisation of Fe in CO/H_2 strongly depends on the iron particle size, i.e. activation energy of carbide formation increases from ca. 110 kJ mol^{-1} to ca. 220 kJ mol^{-1} when the iron particle size decreases from 27 nm to 9 nm [76]. Similar results were found by Cheng et al. indicating stronger carbide formation for larger iron particles [70]. This is in fair agreement with our results showing fast carburisation of $\alpha\text{-Fe}$ (ex $\alpha\text{-Fe}_2\text{O}_3(\text{PVA})$) with relatively large iron crystallites (41 nm) as compared to that (23 nm) obtained from $\gamma\text{-Fe}_2\text{O}_3(\text{n})$. Additionally, it is supposed that the metallic iron phase of $\alpha\text{-Fe}_2\text{O}_3(\text{PVA})$ exhibits a relatively narrow crystallite size distribution, as no change in crystallite size is obtained upon methanation and carburisation, respectively. Moreover, the crystallite size of $\theta\text{-Fe}_3\text{C}$ originated from $\alpha\text{-Fe}_2\text{O}_3(\text{PVA})$ decreases with TOS (78 nm at 60 min, 46 nm at 270 min). Similarly, Shroff et al. demonstrated carbide formation

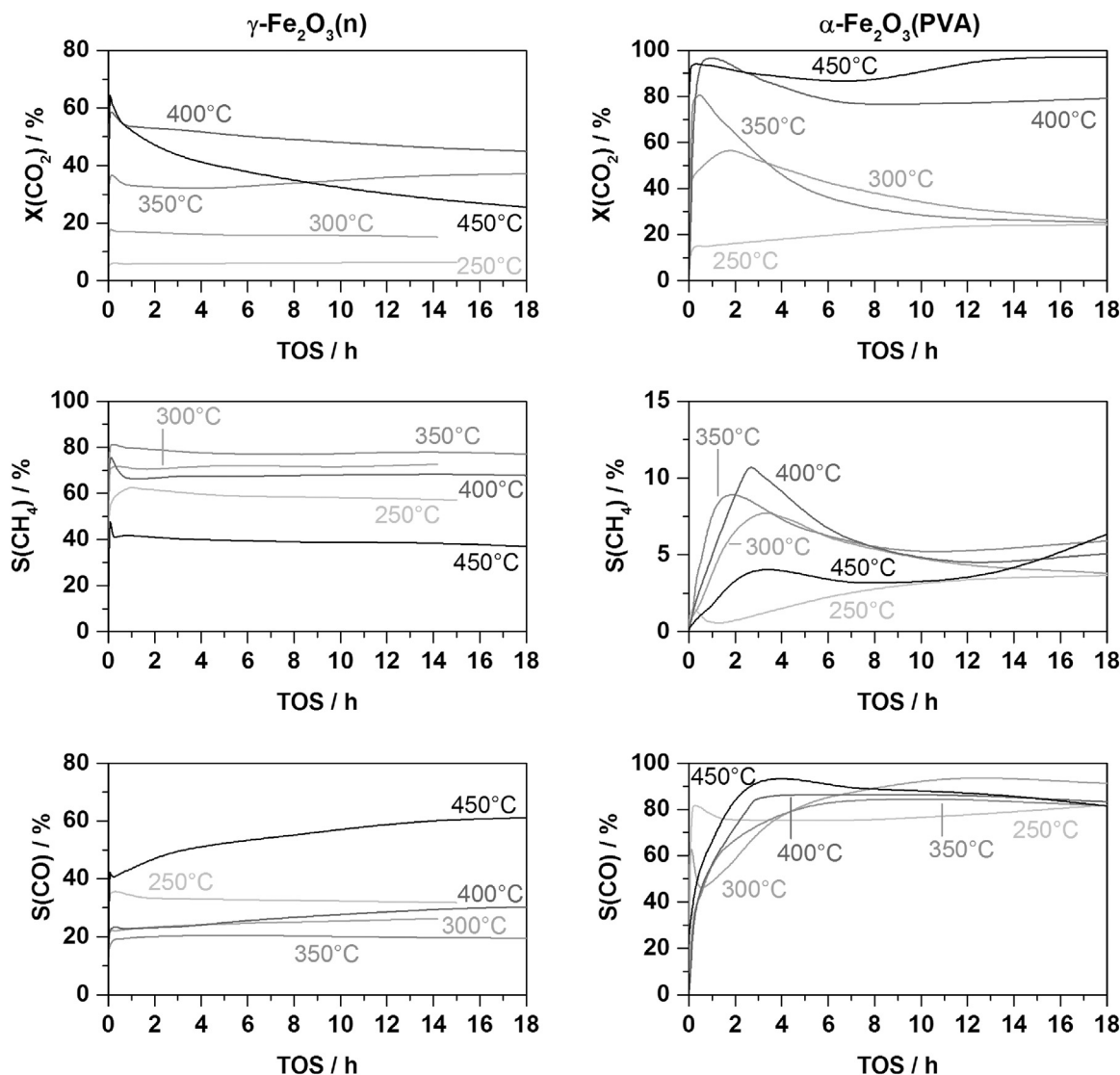


Fig. 7. CO₂ methanation on γ -Fe₂O₃(n) (left) and α -Fe₂O₃(PVA) (right) between 250 °C and 450 °C. Pretreatment: 450 °C for 2 h in 20 vol.% H₂/80 vol.% N₂. Methanation conditions: y(CO₂) = 1000 vppm, y(H₂) = 20 vol.%, N₂ balance, GHSV = 120'000 h⁻¹, p = 1 bar.

during activation of a Fe based FTS catalyst [77]. They found that the initial α -Fe₂O₃ phase is rapidly converted into Fe₃O₄ upon H₂/CO exposure followed by formation of small iron carbide nodules on the catalyst surface. The carbide particles are covered by a layer of amorphous carbon, whereas the Fe₃O₄ surface is devoid of carbon films. Kalakkad et al. [78] described attrition of nano-scaled iron catalysts by incorporation of carbon in the exposure to CO. Therefore, with the cited literature [77,78] it may be speculated that the decrease in crystallite size of θ -Fe₃C (Fig. 9) is related to carbon surrounding the carbide particles thus affecting the microstructure and particle size of the catalyst.

For detailed investigation of the carbonaceous species originated from CO₂ methanation, TPH studies were made after TOS of 2 and 18 h (Fig. 11). The amount of carbon deposited was calculated from integration of the CH₄ traces recorded in TPH. The results are demonstrated in Table 3 along with the corresponding carbon quantities deduced from the mass balance (Fig. 8) both evidencing increase in the carbon deposits with TOS. As already stated above, a much smaller abundance of carbon is found for γ -Fe₂O₃(n). However, the quantities of carbon released in TPH are clearly smaller than that from mass balance, which is notably more pronounced for γ -Fe₂O₃(n). The differences suggest that the carbonaceous species

Table 3

Amount of carbonaceous species (n_C) formed on γ -Fe₂O₃(n) and α -Fe₂O₃(PVA) upon methanation^a at 400 °C for TOS of 2 and 18 h; data are calculated from TPH and carbon mass balance.

	γ -Fe ₂ O ₃ (n)		α -Fe ₂ O ₃ (PVA)	
	TOS = 2 h	TOS = 18 h	TOS = 2 h	TOS = 18 h
$n_{C,TPH}/\mu\text{mol}^b$	104	298	845	2226
$n_{C,massbalance}/\mu\text{mol}^c$	133	678	850	2380

^a Pretreatment conditions: 450 °C for 2 h in 20 vol.% H₂, 80 vol.% N₂. Methanation conditions: y(CO₂) = 1000 vppm, y(H₂) = 20 vol.%, N₂ balance, GHSV = 120'000 h, p = 1 bar.

^b Data taken from Fig. 11.

^c Data taken from Fig. 8.

are not completely converted into CH₄ upon TPH, but also exist in the form of inactive carbon moieties remaining on the catalyst even up to 800 °C. This interpretation is in line with Chun et al. showing hydrogenation of bulk carbon present on a Fe based FTS catalyst in the TPH range from ca. 750 to 900 °C [75].

Furthermore, the carbonaceous species reflected by their specific TPH signal are characterised based on a plausible assignment from Xu et al. [46] distinguishing adsorbed atomic carbon,

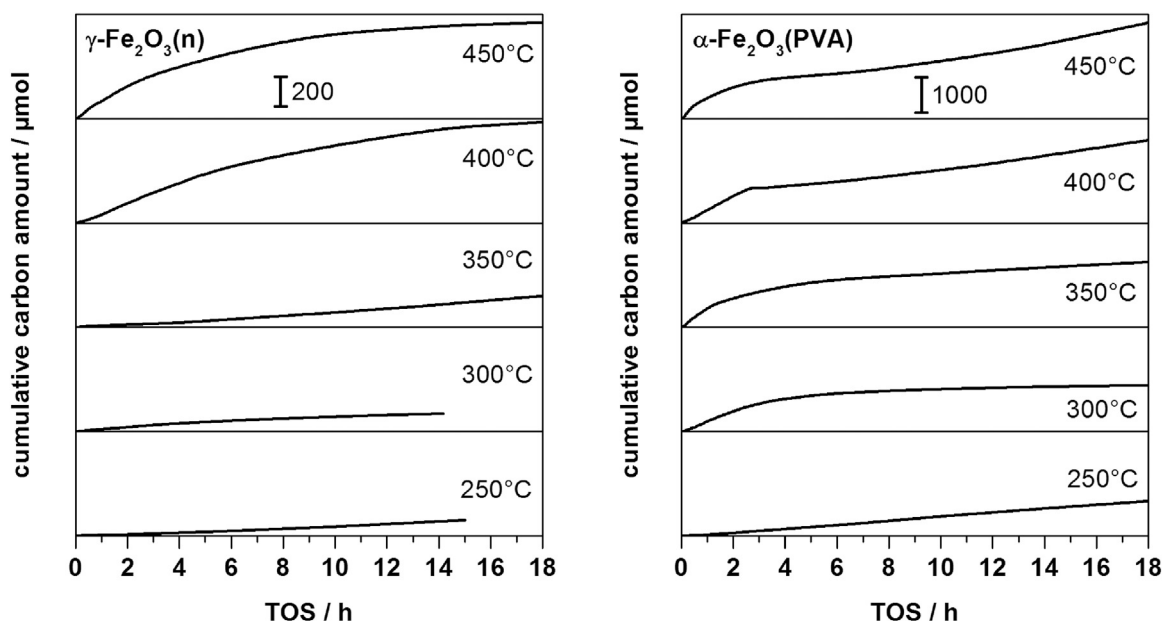


Fig. 8. Carbon accumulation on $\gamma\text{-Fe}_2\text{O}_3(\text{n})$ (left) and $\alpha\text{-Fe}_2\text{O}_3(\text{PVA})$ (right) during CO_2 methanation at temperatures between 250 °C and 450 °C. Pretreatment: 450 °C for 2 h in 20 vol.% H_2 /80 vol.% N_2 . Methanation conditions: $y(\text{CO}_2) = 1000$ vppm, $y(\text{H}_2) = 20$ vol.%, N_2 balance, GHSV = $120'000 \text{ h}^{-1}$, $p = 1$ bar.

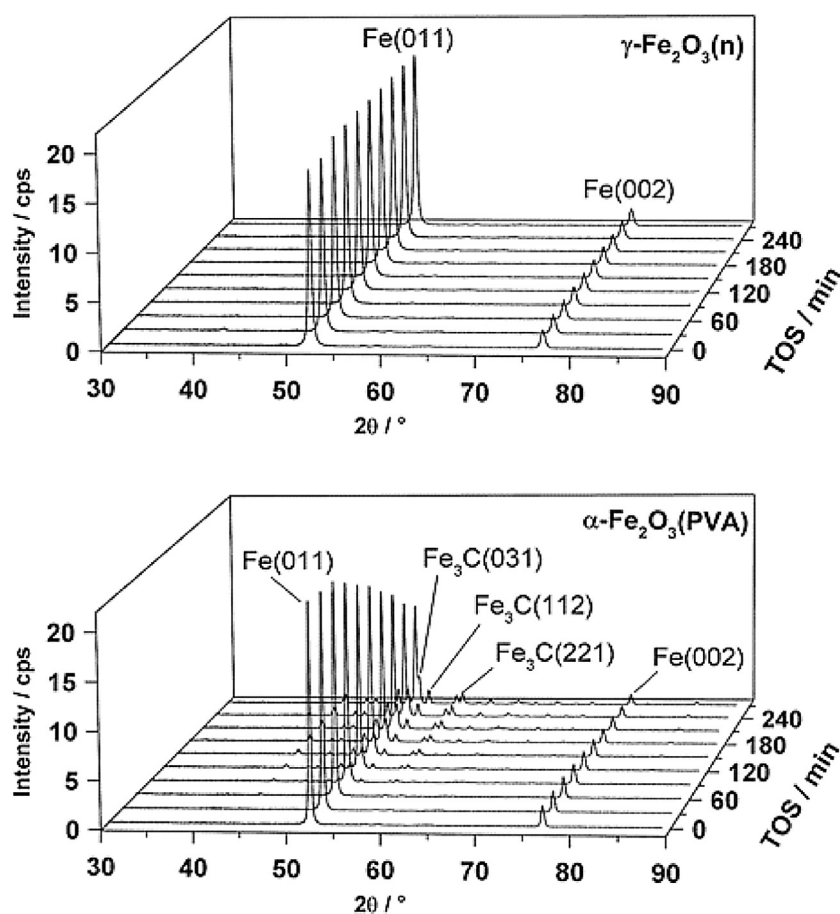


Fig. 9. In situ XRD patterns of $\gamma\text{-Fe}_2\text{O}_3(\text{n})$ (top) and $\alpha\text{-Fe}_2\text{O}_3(\text{PVA})$ (bottom) with time on stream upon CO_2 methanation at 400 °C. Pretreatment: 450 °C in 20 vol.% H_2 /80 vol.% N_2 . Methanation conditions: $y(\text{CO}_2) = 1000$ vppm, $y(\text{H}_2) = 20$ vol.%, N_2 balance, $p = 1$ bar.

polymeric carbon, iron carbides and graphitic carbon. Fig. 11 demonstrates that the TPH profile of prerduced $\gamma\text{-Fe}_2\text{O}_3(\text{n})$ reveals one distinct peak at ca. 300 °C after 2 h methanation. This feature

is attributed to surface carbon species [46], which is consistent with in situ XRD excluding bulk iron carbide. After methanation for 18 h, the TPH signal is more pronounced and broadened towards

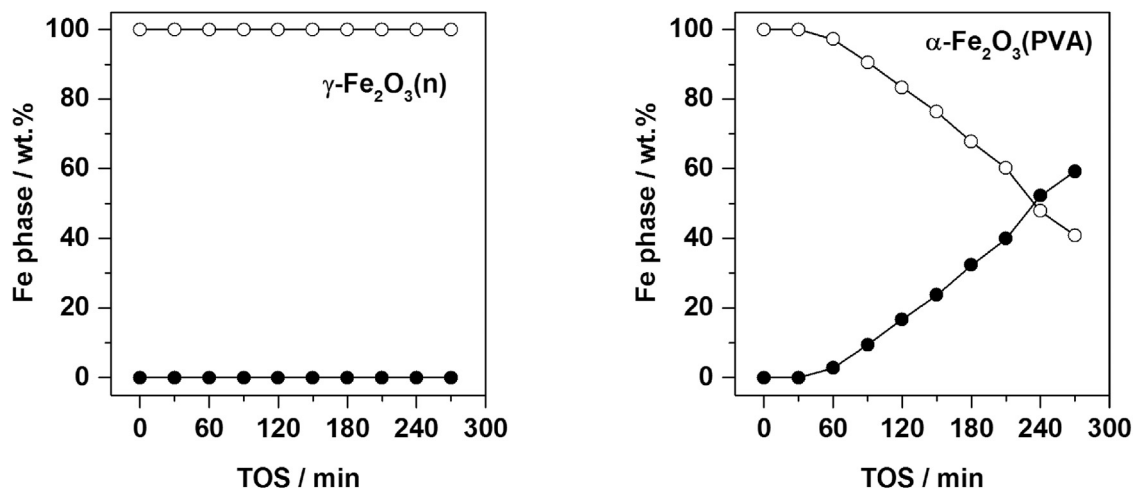


Fig. 10. Fractions of Fe^0 (○) and Fe_3C (●) upon CO_2 methanation at 400 °C on $\gamma\text{-Fe}_2\text{O}_3(\text{n})$ (left) and $\alpha\text{-Fe}_2\text{O}_3(\text{PVA})$ (right). Pretreatment: 450 °C in 20 vol.% H_2 /80 vol.% N_2 . Methanation conditions: $y(\text{CO}_2) = 1000$ vppm, $y(\text{H}_2) = 20$ vol.%, N_2 balance, $p = 1$ bar.

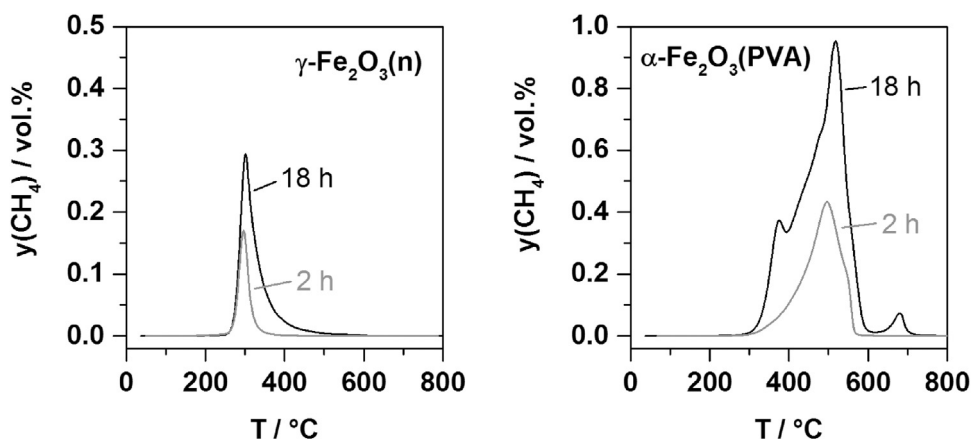


Fig. 11. TPH patterns of $\gamma\text{-Fe}_2\text{O}_3(\text{n})$ (left) and $\alpha\text{-Fe}_2\text{O}_3(\text{PVA})$ (right) after CO_2 methanation at 400 °C for 2 and 18 h. Pretreatment: 450 °C for 2 h in 20 vol.% H_2 /80 vol.% N_2 . Methanation conditions: $y(\text{CO}_2) = 1000$ vppm, $y(\text{H}_2) = 20$ vol.%, N_2 balance, GHSV = 120 000 h^{-1} , $p = 1$ bar. TPH conditions: $F = 200$ ml min^{-1} , $y(\text{H}_2) = 100$ vol.%, $\Delta T/\Delta t = 5$ K min^{-1} .

higher temperatures indicating the formation of less reactive carbon entities. These species are assigned to polymeric surface carbon [46], which is supposed to decrease the conversion of CO_2 at 400 °C (Fig. 7) by covering the catalyst surface.

The TPH pattern of prereduced $\alpha\text{-Fe}_2\text{O}_3(\text{PVA})$ after TOS of 2 h shows a peak at about 500 °C with a shoulder at ca. 545 °C both ascribed to the hydrogenation of iron carbides [46]. This corresponds with the results of in situ XRD indicating carburisation of the elemental iron to form $\theta\text{-Fe}_3\text{C}$. However, the production of additional carbonaceous species, such as polymeric surface carbon, cannot be excluded due to the broad slope on the low temperature side of the TPH feature. After methanation for 18 h the TPH profile clearly grows and shows three peaks located at ca. 375 °C, 515 °C and 680 °C. The new peak at ca. 680 °C is ascribed to rather inactive graphitic bulk carbon [46], which is in accordance with mass balance of carbon (Fig. 8) indicating continuous accumulation of bulk carbon when formation of $\theta\text{-Fe}_3\text{C}$ is completed after approx. 3 h. This, consequently, may lead to the observed decline in CO_2 conversion (Fig. 7) by mechanically blocking active sites as described in literature [45]. Moreover, the carbon amount related to the pronounced peak at 515 °C (ca. 2170 μmol) is approx. 2.5 times stronger than the carbon quantity needed for Fe_3C formation (ca. 830 μmol) evidencing presence of bulk and/or surface carbon species in this TPH regime as well. The TPH feature at 375 °C may be associated with the decreasing crystallite size of $\theta\text{-Fe}_3\text{C}$ found by

in situ XRD. Chernavskii et al. discussed that peak temperature for hydrogenation of iron carbide declines from 380 °C to 336 °C when the carbide particle size decreases from 27 nm to 9 nm [76]. Furthermore, formation of polymeric surface carbon might also occur in this temperature regime as previously reported for $\gamma\text{-Fe}_2\text{O}_3(\text{n})$. However, due to the relatively large intensity of the TPH peak at 375 °C it is more likely that CH_4 formation is mainly attributed to hydrogenation of $\theta\text{-Fe}_3\text{C}$.

The correlation of the CO_2 methanation performance of the catalysts with their chemical composition obtained from XRD, TPH and carbon mass balance suggests that the substantial efficiency of $\gamma\text{-Fe}_2\text{O}_3(\text{n})$ is tentatively referred to the presence of surface carbon species revealing strongest hydrogenation activity upon TPH. Contrary, rather minor contribution is assumed for metallic iron, since the presence of Fe^0 evokes only little CH_4 formation as shown in the tests with prereduced $\alpha\text{-Fe}_2\text{O}_3(\text{PVA})$. Negligible methanation efficiency is also ascribed to the iron carbide and bulk carbon species, which predominately exist in the weakly active $\alpha\text{-Fe}_2\text{O}_3(\text{PVA})$.

3.6. CO_2 methanation activity of prereduced $\gamma\text{-Fe}_2\text{O}_3(\text{n})$ catalyst under practical conditions

For more practical assessment of the best catalyst tested, additional CO_2 hydrogenation studies were conducted at 400 °C by using prereduced $\gamma\text{-Fe}_2\text{O}_3(\text{n})$. In these investigations, the CO_2

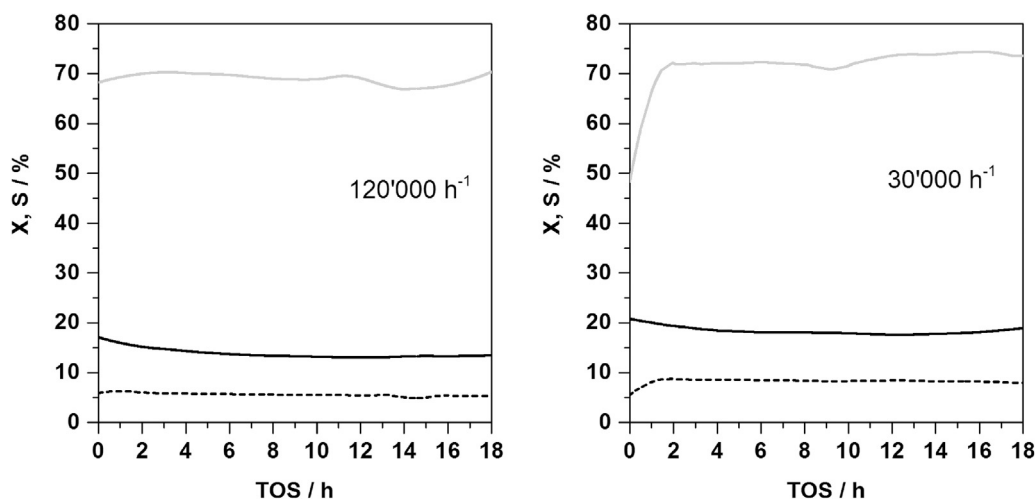


Fig. 12. CO₂ methanation performance of γ -Fe₂O₃(n) at 400 °C for GHSV of 120'000 h⁻¹ (left) and 30'000 h⁻¹ (right) (X(CO₂) (—), S(CH₄) (---), S(CO) (···)). Pretreatment: 450 °C for 2 h in 20 vol.% H₂/80 vol.% N₂. Methanation conditions: y(CO₂) = 10 vol.%, y(H₂) = 40 vol.%, y(N₂) = 50 vol.%, p = 1 bar.

fraction was 10 vol.% with a stoichiometric H₂/CO₂ ratio of 4. Exemplarily, such feed composition is of relevance for methanation of biogas CO₂. Moreover, the space velocity was varied to 120,000 h⁻¹ and 30,000 h⁻¹ referring to a catalyst mass of 200 and 800 mg, respectively. Again, in the catalytic studies the difference between inlet and outlet temperature was found smaller than 10 K and no pressure drop occurred. Fig. 12 indicates that with 10 vol.% CO₂ only little conversion occurs in contrast to the study with 1000 vppm CO₂. At the space velocity of 120,000 h⁻¹ the maximum CO₂ conversion is ca. 17% and is achieved in the initial stage of methanation implying a CH₄ selectivity of approx. 6%. When decreasing the space velocity to 30,000 h⁻¹ the conversion of CO₂ and selectivity of CH₄ go up to 20% and 8%, respectively, associated with longer residence time of the feed in the catalyst bed. This corresponds to an increase in CH₄ production rate from $2.64 \cdot 10^{-7} \text{ mol s}^{-1}$ at 120,000 h⁻¹– $5.54 \cdot 10^{-7} \text{ mol s}^{-1}$ at 30,000 h⁻¹. Note that limitation of the catalytic conversion by film and pore diffusion is to be excluded by checking Mears and Weisz-Prater criteria [79,80].

Furthermore, a crucial feature of the tests with increased feed content of CO₂ is the major genesis of CO according to RWGS representing the favoured pathway. Contrary, in the tests with 1000 vppm CO₂, CH₄ is yielded as the main product on γ -Fe₂O₃(n). However, the rather little production of CH₄ is not only a result of the increased flow of CO₂, but is also referred to the stoichiometric H₂/CO₂ ratio (4:1), whereas in the examinations with 1000 vppm CO₂ a strong excess of H₂ (200:1) was used.

Additionally, in the presence of 10 vol.% CO₂ little production of ethane, ethene, propane and propene is also observed amounting to a total selectivity of approx. 2% (120,000 h⁻¹) and 3% (30,000 h⁻¹). Based on the formation of CH₄, CO, C₂ and C₃ hydrocarbons at TOS of 18 h an overall selectivity of gaseous products of about 80% is obtained suggesting strong accumulation of carbon on the catalyst. For characterisation of the carbon deposits, the catalyst evaluated at a space velocity of 120,000 h⁻¹ was checked by XRD and TPH after 18 h methanation. Quantitative XRD analysis shows complete conversion of the original iron component into iron carbides with a phase composition of 88 wt.% cementite-type θ -Fe₃C and 12 wt.% Haegg-type χ -Fe₅C₂; the simultaneous existence of both carbide phases is in line with the literature [81]. The presence of the iron carbides evidences carburisation of the iron, whereas in the studies with 1000 vppm CO₂ no carbide formation was found (Section 3.5). This strong carbon incorporation is additionally confirmed by TPH providing a quantity of 1725 $\mu\text{mol C}$; in presence of 1000 vppm CO₂ it is 298 μmol only (Table 3). The TPH profile

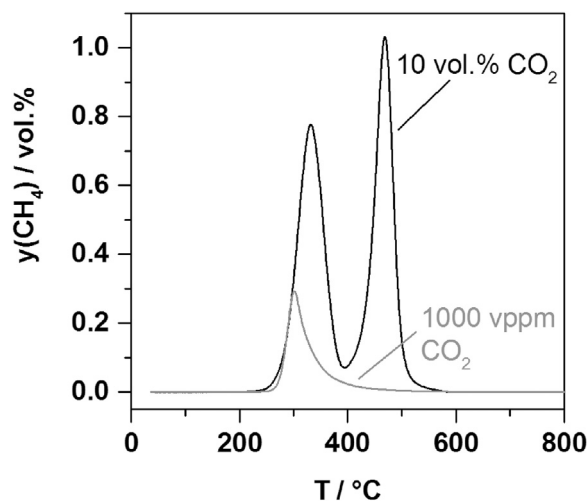


Fig. 13. TPH patterns of γ -Fe₂O₃(n) after CO₂ methanation at 400 °C with 10 vol.% CO₂/40 vol.% H₂ and 1000 vppm CO₂/20 vol.% H₂ (data from Fig. 11). Pretreatment: 450 °C for 2 h in 20 vol.% H₂/80 vol.% N₂. Methanation conditions: GHSV = 120'000 h⁻¹, p = 1 bar. TPH conditions: F = 200 ml min⁻¹, y(H₂) = 100 vol.%, $\Delta T/\Delta t = 5 \text{ K min}^{-1}$.

recorded after CO₂ hydrogenation is demonstrated in Fig. 13, which also shows the trace obtained for reaction with the low CO₂ proportion. After methanation in presence of 10 vol.% TPH peaks are observed at 330 °C and 470 °C. The first feature is slightly shifted to higher temperatures as referred to the test with 1000 vppm CO₂, while the second one additionally appears. For unambiguous assignment, an additional TPH experiment was made, which was stopped at 400 °C followed by XRD and Moessbauer spectroscopic analysis. For the latter investigations, the sample was passivated by adjusting a flow of 1 vol.% O₂ and 99 vol.% N₂ at room temperature. As a result, both analytical tools indicate exclusive presence of α -Fe (Fig. 14); the corresponding Moessbauer parameters are $\delta = 0.0 \text{ mm s}^{-1}$, $E_Q = 0.0 \text{ mm s}^{-1}$ and $H_{\text{hf}} = 331 \text{ kOe}$. Therefore, the low-temperature TPH signal is assigned to the bulk iron carbides found by XRD prior to TPH. The proportion of carbon corresponding to this peak is equal to ca. 865 μmol . This quantity is in good agreement with the crystalline composition derived from XRD implying a carbon amount of 855 μmol . It should be noticed that the assignment of the first TPH signal to iron carbides differs from that often published in the literature [46,75]. However, the tem-

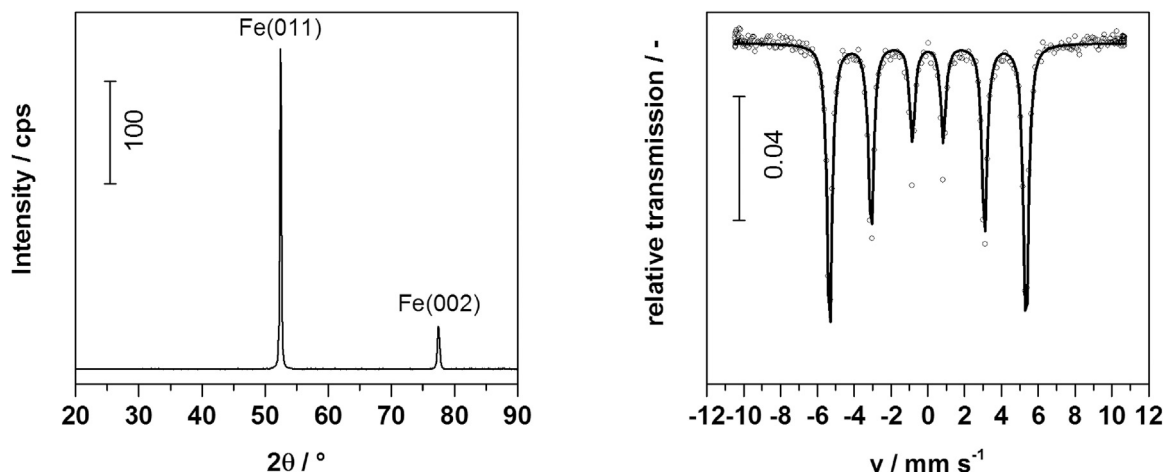


Fig. 14. XRD pattern (left) and Moessbauer spectra (right) of $\gamma\text{-Fe}_2\text{O}_3(\text{n})$ after CO_2 methanation and subsequent TPH stopped at 400°C . Reaction conditions are given in Fig. 13.

perature regimes reported are very broad going up to ca. 690°C depending on catalyst properties and TPH conditions. Finally, the TPH signal located at higher temperatures is interpreted with bulk carbon amounting to ca. $860\ \mu\text{mol}$. Due to its clearly lower hydrogenation activity referred to the iron carbides it is assumed that the contribution of these bulk carbon species to the methanation performance is rather minor. Also, despite the significant deposition of carbon a deactivation of the catalyst, i.e. the iron carbide entities, is hardly observed with time on stream (Fig. 12). Finally, it is evident that in the presence of 10 vol.% CO_2 and stoichiometric H_2/CO_2 ratio the carburisation and formation of inactive carbon is more favoured than the methanation reaction [82].

Furthermore, for comparison purposes, a hydrogenation study was conducted with a home-made $\text{Ni}/\gamma\text{-Al}_2\text{O}_3$ catalyst revealing a Ni load of 20 wt.%. The investigation was carried out under the same reaction conditions as for $\gamma\text{-Fe}_2\text{O}_3(\text{n})$, i.e. 400°C , $120,000\ \text{h}^{-1}$, 10 vol.% CO_2 and 40 vol.%. The test shows a CO_2 conversion of 64% and a CH_4 selectivity of 80% indicating clearly higher methanation activity as referred to the present Fe based catalysts. It has to be stated that the performance of the $\text{Ni}/\gamma\text{-Al}_2\text{O}_3$ reference is typical for the reaction conditions established as referred to Ni catalysts reported in the literature [13]. Nevertheless, the CH_4 production of $\gamma\text{-Fe}_2\text{O}_3(\text{n})$ referring to 400°C and $30,000\ \text{h}^{-1}$ lies in a similar range reported for bare iron carbide catalysts [26].

4. Conclusion

The objective of this paper was the evaluation of iron oxide precursors for the CO_2 hydrogenation to CH_4 and H_2O under atmospheric pressure conditions. Thus, a series of several iron based catalyst was screened including physical-chemical characterisation. The best catalyst was the $\gamma\text{-Fe}_2\text{O}_3(\text{n})$ sample achieving maximum CH_4 yield of 59% at 400°C at a molar H_2/CO_2 ratio of 200. In methanation, all catalysts revealed significant accumulation of carbon. Detailed studies of structure and reactivity of these carbonaceous species were performed for $\gamma\text{-Fe}_2\text{O}_3(\text{n})$ and $\alpha\text{-Fe}_2\text{O}_3(\text{PVA})$. It was found that the quantity of the different types of carbon species, i.e. surface carbon, iron carbides and bulk carbon, crucially depends on the properties of the catalyst. More specifically, fast carburisation was observed for relatively large iron crystallites obtained from $\alpha\text{-Fe}_2\text{O}_3(\text{PVA})$ as compared to that of $\gamma\text{-Fe}_2\text{O}_3(\text{n})$. The relatively high methanation activity of $\gamma\text{-Fe}_2\text{O}_3(\text{n})$ was attributed to the abundance of surface carbon species, whereas less reactive iron carbides and bulk carbon were formed on $\alpha\text{-Fe}_2\text{O}_3(\text{PVA})$ leading to significantly lower CH_4 formation.

When performing hydrogenation with a CO_2 proportion of 10 vol.% and stoichiometric H_2/CO_2 ratio a relatively strong CO production appeared due to the reverse water gas shift reaction. At 400°C and $120,000\ \text{h}^{-1}$ a CO_2 conversion of 17% and CH_4 selectivity of 6% was achieved on $\gamma\text{-Fe}_2\text{O}_3(\text{n})$. Decrease in GHSV to $30,000\ \text{h}^{-1}$ led to slightly inclining CO_2 conversion and CH_4 selectivity amounting to 20% and 8%, respectively. Under these conditions iron carbides were responsible for the catalytic performance, while deposition of inactive bulk carbon occurred upon methanation. As a conclusion, the present study suggests that CO_2 hydrogenation on Fe catalysts is strongly affected by the feed concentration of CO_2 leading to formation of different types of carbon species with specific methanation activity. In future work, the catalysts will be evaluated under higher pressures and lower GHSV to further screen the potential of bare iron based catalysts for hydrogenation of CO_2 .

Acknowledgements

The authors thankfully acknowledge the financial support from the Agency of Renewable Resources and the Federal Ministry of Food and Agriculture under the project Effekt (22400313). Additionally, the cooperation with DBI-GTI is acknowledged with gratitude.

References

- [1] BP, Statistical Review of World Energy, 63rd edition, 2014, June.
- [2] C. Song, Catal. Today 115 (2006) 2.
- [3] A.C. Köne, T. Büke, Ren. Sust. Energy Rev. 14 (2010) 2906.
- [4] R.F. Keeling, S.J. Walker, S.C. Piper, A.F. Bollenbacher, Scripps CO_2 Program, (<http://scrippsco2.ucsd.edu/>), Scripps Institution of Oceanography Atmospheric CO_2 concentrations derived from in situ air measurements at Mauna Loa, Hawaii.
- [5] T. Bruhn, H. Naims, B. Olfe-Kräutlein, Env. Sci. Pol. 60 (2016) 38.
- [6] L. Li, N. Zhao, W. Wei, Y. Sun, Fuel 108 (2013) 112.
- [7] S.S. Nam, H. Kim, G. Kishan, M.-J. Choi, K.-W. Lee, Appl. Catal. A 179 (1999) 155.
- [8] C.-K. Kuei, M.-D. Lee, Can. J. Chem. Eng. 69 (1991) 347.
- [9] P. Sabatier, J.B. Senderens, Acad. Sci. 134 (1902) 689.
- [10] G. Gahleitner, Int. J. Hydrogen Energy 38 (2013) 2039.
- [11] S. Bajohr, D. Schollenberger, D. Buchholz, T. Weinfurter, M. Götz, gwf—Gas + Energie, 155, 2014, pp. 470.
- [12] Gas production, 3. gas treating Ullmann's Encyclopedia of Industrial Chemistry, Vol. 16, Wiley-VCH, 2010, 491.
- [13] W. Wang, J. Gong, Front. Chem. Sci. Eng. 5 (2011) 2.
- [14] S. Tada, T. Shimizu, H. Kameyama, T. Haneda, R. Kikuchi, Int. J. Hydrogen Energy 37 (2012) 5527.
- [15] Y. Wang, R. Wu, Y. Zhao, Catal. Today 158 (2010) 470.
- [16] B. Mutz, H.W.P. Carvalho, S. Mangold, W. Kleist, J.-D. Grunwaldt, J. Catal. 327 (2015) 48.
- [17] S. Rahmani, M. Rezaei, F. Meshkani, J. Ind. Eng. Chem. 20 (2014) 1346.
- [18] M. Kusmierz, Catal. Today 137 (2008) 429.

- [19] S. Tada, O.J. Ochieng, R. Kikuchi, T. Haneda, H. Kameyama, *Int. J. Hydrogen Energy* 39 (2014) 10090.
- [20] Z. Kowalczyk, K. Stolecki, W. Raróg-Pilecka, E. Miskiewicz, E. Wilczkowska, Z. Karpinski, *Appl. Catal. A* 342 (2008) 35.
- [21] I.A. Fisher, A.T. Bell, *J. Catal.* 162 (1996) 54.
- [22] F. Solymosi, A. Erdöhelyi, T. Bánsági, *J. Catal.* 68 (1981) 371.
- [23] D.W. Goodman, D.E. Peebles, J.M. White, *Surf. Sci.* 140 (1984) L239.
- [24] A.N. Akin, Z.I. Önsan, *J. Chem. Tech. Biotechnol.* 69 (1997) 337.
- [25] G. Zhou, T. Wu, H. Xie, X. Zheng, *Int. J. Hydrogen Energy* 38 (2013) 10012.
- [26] M.-D. Lee, J.-F. Lee, C.-S. Chang, *J. Chem. Eng. Japan* 23 (1990) 130.
- [27] T. Yoshida, K. Nishizawa, M. Tabata, H. Abe, T. Kodama, M. Tsuji, Y. Tamaura, *J. Mat. Sci.* 28 (1993) 1220.
- [28] M. Tsuji, K. Nishizawa, T. Yoshida, Y. Tamaura, *J. Mat. Sci.* 29 (1994) 5481.
- [29] J. Fournier, L. Carreiro, Y.-T. Qian, S. Soled, R. Kershaw, K. Dwight, A. Wold, *J. Solid State Chem.* 58 (1985) 211.
- [30] A.L. Kustov, A.M. Frey, K.E. Larsen, T. Johannessen, J.K. Nørskov, C.H. Christensen, *Appl. Catal. A* 320 (2007) 98.
- [31] V.M. Vlasenko, G.E. Yuzefovich, *Russ. Chem. Rev.* 38 (1969) 728.
- [32] M. Jacquemin, A. Beuls, P. Ruiz, *Catal. Today* 157 (2010) 462.
- [33] D.E. Peebles, D.W. Goodman, J.M. White, *J. Phys. Chem.* 87 (1983) 4378.
- [34] M. Marwood, R. Doepper, A. Renken, *Appl. Catal. A* 151 (1997) 223.
- [35] C. Schild, A. Wokaun, R.A. Koeppe, A. Baiker, *J. Phys. Chem.* 95 (1991) 6341.
- [36] F. Ocampo, B. Louis, L. Kiwi-Minsker, A.-C. Roger, *Appl. Catal. A* 392 (2011) 36.
- [37] T.T.M. Nguyen, L. Wissing, M.S. Skjøth-Rasmussen, *Catal. Today* 215 (2013) 233.
- [38] S. Hwang, U.G. Hong, J. Lee, J.H. Baik, D.J. Koh, H. Lim, I.K. Song, *Catal. Lett.* 142 (2012) 860.
- [39] C.G. Visconti, M. Martinelli, L. Falbo, L. Fratolocchi, L. Lietti, *Catal. Today* 277 (2016) 161.
- [40] E. de Smit, B.M. Weckhuysen, *Chem. Soc. Rev.* 37 (2008) 2758.
- [41] B.R.J. Smith, M. Loganathan, M.S. Shantha, *Int. J. Chem. Reactor Eng.* 8 (2010) (Review R4).
- [42] Ammonia, 2. production processes Ullmann's Encyclopedia of Industrial Chemistry, Vol. 3, Wiley-VCH, 2010 (139).
- [43] E. de Smit, A.M. Beale, S. Nikitenko, B.M. Weckhuysen, *J. Catal.* 262 (2009) 244.
- [44] M. Ding, Y. Yang, B. Wu, T. Wang, L. Ma, H. Xiang, Y. Li, *J. Mol. Catal. A* 351 (2011) 165.
- [45] C.H. Bartholomew, *Appl. Catal. A* 212 (2001) 17.
- [46] J. Xu, C.H. Bartholomew, *J. Phys. Chem. B* 109 (2005) 2392.
- [47] T. Herranz, S. Rojas, F.J. Pérez-Alonso, M. Ojeda, P. Terreros, J.L.G. Fierro, *J. Catal.* 243 (2006) 199.
- [48] P. Balle, B. Geiger, S. Kureti, *Appl. Catal. B* 85 (2009) 109.
- [49] S. Wagloehner, J.N. Baer, S. Kureti, *Appl. Catal. B* 147 (2014) 1000.
- [50] S. Kureti, W. Weisweiler, K. Hizbullah, *Appl. Catal. B* 43 (2003) 281.
- [51] S.K. Saha, P. Pramanik, *Nanostr. Mater.* 8 (1997) 29.
- [52] B.D. Cullity, *Elements of X-Ray Diffraction*, Addison-Wesley Publishing Company, Reading, Massachusetts, 1956.
- [53] H.M. Rietveld, *Acta Cryst.* 22 (1967) 151.
- [54] B.H. Toby, *Powder Diff.* 21 (2006) 67.
- [55] E.P. Barrett, L.G. Joyner, P.P. Halenda, *J. Am. Chem. Soc.* 73 (1951) 373.
- [56] R. Qin, F. Li, W. Jiang, L. Liu, *J. Mater. Sci. Technol.* 25 (2009) 69.
- [57] J.Y. Park, D. Patel, E.S. Choi, M.J. Baek, Y. Chang, T.J. Kim, G.H. Lee, *Colloids Surf. A* 367 (2010) 41.
- [58] H. Shechter, P. Hillman, M. Ron, *J. Appl. Phys.* 37 (1966) 3043.
- [59] A. Pattek-Janczyk, B. Miczko, *Sol. State Ionics* 58 (1992) 249.
- [60] A. Pattek-Janczyk, J.-C. Grenier, B. Miczko, *Sol. State Ion.* 117 (1999) 95.
- [61] L. Minervini, R.W. Grimes, *J. Phys. Chem. Sol.* 60 (1999) 235.
- [62] E. Kuzmann, S. Nagy, A. Vértés, *Pure Appl. Chem.* 75 (2003) 801.
- [63] A. Pattek-Janczyk, *Sol. State Ion.* 38 (1990) 171.
- [64] L.F. Checherskaya, V.P. Romanov, P.A. Tatsienko, *Phys. Stat. Sol. (a)* 19 (1973) K177.
- [65] K. Woo, J. Hong, S. Choi, H.-W. Lee, J.-P. Ahn, C.S. Kim, S.W. Lee, *Chem. Mater.* 16 (2004) 2814.
- [66] S. Brunauer, L.S. Deming, W.S. Deming, E. Teller, *J. Am. Chem. Soc.* 62 (1940) 1723.
- [67] F. Adam, J. Andas, I.A. Rahman, *Chem. Eng. J.* 165 (2010) 658.
- [68] F. Meshkani, M. Razaee, *Chem. Eng. Res. Des.* 95 (2015) 288.
- [69] M. Thommes, *Chem. Ing. Tech.* 82 (2010) 1059.
- [70] K. Cheng, M. Virginie, V.V. Ordonsky, C. Cordier, P.A. Chernavskii, M.I. Ivantsov, S. Paul, Y. Wang, A.Y. Khodakov, *J. Catal.* 328 (2015) 139.
- [71] Ullmann's Encyclopedia of Industrial Chemistry, Vol. 16, Wiley-VCH, 2010, Coal Liquefaction, 2.2 Fischer-Tropsch Synthesis, 20.
- [72] D.S. Newsome, *Catal. Rev. Sci. Eng.* 21 (1980) 275.
- [73] M.D. Shroff, D.S. Kalakkad, K.E. Coulter, S.D. Köhler, M.S. Harrington, N.B. Jackson, A.G. Sault, A.K. Datye, *J. Catal.* 156 (1995) 185.
- [74] I.O. Pérez De Berti, J.F. Bengoa, S.J. Stewart, M.V. Cagnoli, G. Pecchi, S.G. Marchetti, *J. Catal.* 335 (2016) 36.
- [75] D.H. Chun, J.C. Park, S.Y. Hong, J.T. Lim, C.S. Kim, H.-T. Lee, J.-I. Yang, S. Hong, H. Jung, *J. Catal.* 317 (2014) 135.
- [76] P.A. Chernavskii, V.I. Zaikovskii, G.V. Pankina, *Russ. J. Phys. Chem. A* 86 (2012) 1274.
- [77] M.D. Shroff, D.S. Kalakkad, M.S. Harrington, N.B. Jackson, K.E. Coulter, A.G. Sault, A.K. Datye, *The chemistry of transition metal carbides and nitrides*, Blackie Academic & Professional, London, 1996, pp. 511.
- [78] D.S. Kalakkad, M.D. Shroff, S. Köhler, N. Jackson, A.K. Datye, *Appl. Catal. A* 133 (1995) 335.
- [79] D.E. Mears, *Ind. Eng. Chem. Process. Des. Dev.* 10 (1971) 541.
- [80] P.B. Weisz, C.D. Prater, *Adv. Catal.* 6 (1954) 143.
- [81] E. de Smit, F. Cinquini, A.M. Beale, O.V. Safonova, W. van Beek, P. Sautet, B.M. Weckhuysen, *J. Am. Chem. Soc.* 132 (2010) 14928.
- [82] J.W. Niemantsverdriet, A.M. Van der Kraan, *J. Catal.* 72 (1981) 385.